Magnetic Hysteresis Cycle Measurements With a New Needle Probe Setup

Patrick Fagan, Abdellahi Abderahmane, Mathieu Domenjoud, and Laurent Daniel

***Abstract*— Different magnetic needle probe setups are presented, and their strengths and weaknesses are investigated. A new configuration, combining the advantages of the other setups, is presented. Finite element (FE) simulations are implemented to explore the effect of the excitation yokes and residual stresses on the magnetic flux symmetry. The error sources affecting the accuracy of the experimental measurements are analyzed and quantified. Solutions to minimize these errors are also proposed. By minimizing error sources, the obtained experimental measurements closely follow the reference hysteresis loop obtained from a wrapping coil in the unidirectional case. The proposed measurement device notably provides enhanced accuracy for surface measurements when wrapping coils are not implementable.**

***Index Terms*— Induction measurement, magnetic hysteresis, material characterization, nondestructive testing.**

I. Introduction

WHEN subjected to a varying magnetic field, ferromagnetic materials exhibit a typical hysteresis magnetization curve. The magnetic induction versus magnetic field loop is characterized by several properties (coercive field, remanent induction, and hysteresis losses) that play a crucial role in a great number of industrial applications [1], [2]. For example, hysteresis losses (given by the area of the magnetic hysteresis loop) are key to electrical machine performance. A precise experimental measurement of the magnetic hysteresis loop is therefore required for a great number of applications. A precise experimental determination of the magnetic response is therefore indispensable in a number of applications. Many sensors, such as Hall sensors, H-coils, AMR, TMR, or GMR sensors, are available for the measurement of magnetic fields. This article is dedicated to the measurement of magnetic induction.

Received 27 June 2024; revised 22 September 2024; accepted 20 October 2024. Date of publication 21 November 2024; date of current version 4 December 2024. This work was supported in part by the French Agence Nationale de la Recherche (ANR) under Grant ANR-22-CE42-0029-01 and in part by the Project-ENCORE- under Grant ANR-22-CE05-0032-03 (Project PIMCOMAP). The Associate Editor coordinating the review process was Dr. Libing Bai. *(Corresponding author: Patrick Fagan.)*

The authors are with the Université Paris-Saclay, CentraleSupélec, CNRS, Laboratoire de Génie Électrique et Électronique de Paris, 91192 Gif-sur-Yvette, France, and also with the Sorbonne Université, CNRS, Laboratoire de Génie Électrique et Électronique de Paris, 75252 Paris, France (e-mail: patrick.fagan@centralesupelec.fr; abdellahi.abderahmane@centralesupelec.fr; mathieu.domenjoud@centralesupelec.fr; laurent.daniel@centralesupelec.fr).

This article has supplementary downloadable material available at https://doi.org/10.1109/TIM.2024.3502799, provided by the authors.

Digital Object Identifier 10.1109/TIM.2024.3502799

The wrapping coil (B-coil) is one of the standard induction measurement methods due to its simple experimental setup and good signal-to-noise ratio [3]. A coil with a known number of turns is wound around a sample, usually of rectangular or circular cross section. The time variation of the magnetic flux inside the sample generates an induced voltage in the coil. This voltage is proportional to the number of turns; hence, if a stronger signal is needed a longer coil can be wound around the sample. However, the measurement is sensitive only to the component of the magnetic flux density perpendicular to the coil cross section. The measurement is therefore sensitive to one direction in space only. Additionally, B-coil measurements provide an average magnetic flux density across the cross section. Standard samples typically feature a small cross section to ensure uniform induction in the sample cross section. While drilling holes allow for the deployment of wrapping coils on large samples [4], [5], [6], [7], they alter both magnetic and mechanical states [8].

The needle probe method can be used for the nondestructive evaluation of the magnetic properties of a ferromagnetic sample. The wrapping coil is replaced by two conductive probes touching the surface of the sample. This setup is equivalent to a wrapping coil of one turn [9], [10]. It only requires electrical contact between the measurement probes and the sample surface. As a result, it can be used on large samples without drilling holes. However, the main disadvantage is that the signal-to-noise ratio cannot be improved as easily as for the wrapping coil method. Hence, the needle probe method requires low-noise amplifiers and a precisely defined experimental setup in order to obtain a reliable measurement.

This article presents different needle probe setups and their main assumptions. The error sources on the experimental setup are studied in order to minimize them. An example of measurement following the prescribed protocol illustrates the correspondence between wrapping coil and needle probe measurements in a specific case, showing that the two magnetic measurement systems are equivalent in the chosen reference case. The article is structured as follows.

1) Section II describes different needle probe configurations found in the literature and presents a novel setup allowing for more precise measurements.
2) Section III provides finite element (FE) simulations to shed light on the critical factors for needle probe design.
3) Section IV gives the equations linking the measured voltages to the magnetic flux variations inside the sample.

4) Section V is dedicated to the analysis of error sources in the proposed setup and their correction.
5) Section VI describes the practical implementation of the experimental setup.
6) Section VII presents and discusses the experimental measurements.

II. Different Needle Probe Setups

The principle of the needle probe method is derived from Maxwell–Faraday's law. Given a surface S of boundary ∂S, the line integral of the electric field $\vec{E}$ on ∂S is opposite to the surface integral of the scalar product between the surface normal $\vec{n}$ and the derivative of the magnetic induction $\vec{B}$ across the surface S

$$\oint_{\partial S} \vec{E} \cdot \vec{dl} = -\int\int_{S} \frac{\partial \vec{B}}{\partial t} \cdot \vec{n} dS. \tag{1}$$

Hence, by connecting two conductive probes to the sample surface, the induced voltage between the two allows to measure the variation of the magnetic flux in the sample. Since the probes only need to touch the sample, the needle probe method allows for flexible setups and noninvasive multidimensional measurements.

This method has been patented in the 1950s by Czeija and Zawischa [9], Werner [10], and Stauffer [11]. The very weak amplitude of the measured voltages requires strong amplifications to precisely measure the magnetic flux variation in the material. Theoretical studies have been carried out [12], [13], [14], [15], [16], [17] to better evaluate uncertainty sources and alternative setups [14], [18] have been devised to minimize these uncertainties. The magnetic needles method has since been employed in a variety of materials [19], [20] for the measurement of rotational losses [21] and defect detection [22].

Four different setups have been identified in the literature, and each of them is described in this article. These setups are shown in Fig. 1. They are denoted as follows.

1) The original setup (OS), described by Czeija and Zawischa [9] and Werner [10] in their patents, in which a pair of needle probes is placed on each side of the sample, hence giving two voltages V_t and V_b.
2) The single-side OS (SSOS), patented by Czeija and Zawischa [9] and Stauffer [11], Tompkins et al. [12], which has then been employed in the subsequent decades [23]. This setup is a simplified OS, in which the measurement on the bottom face has been removed. As a result, the change in magnetization within the sample can be measured using a single voltage V, under the assumption that the magnetic flux in the sample is symmetrical.
3) The air flux compensation setup (AFCS) [18], derived from the SSOS by adding a pair of needles that are short-circuited, but insulated from the sample. Two voltage measurements are required to describe the magnetic flux variation in one direction: the voltage in the sample V_{sample} and the air voltage V_{air}.
4) The transverse needle probe setup (TNPS) [14], in which two pairs of needle probes are placed in the same fashion as in the OS, but the voltages are measured in a differential configuration.

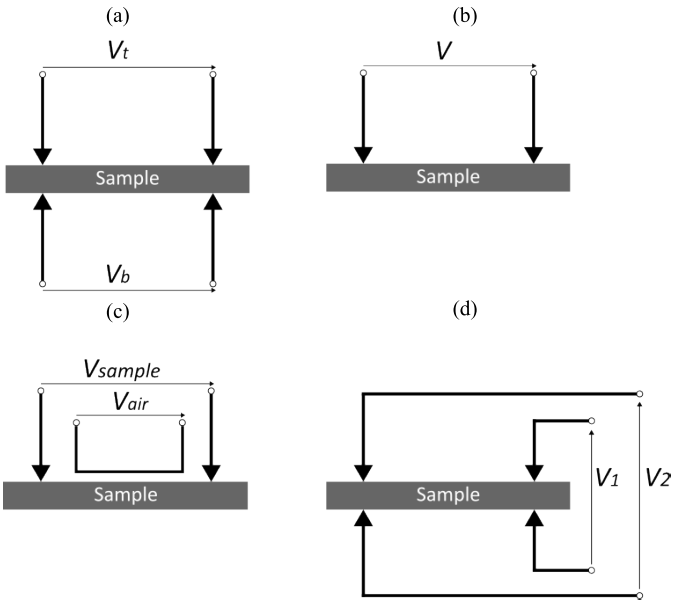

Fig. 1. Four different methods for needle probe measurements described in this article. (a) OS. (b) SSOS. (c) AFCS. (d) TNPS.

Fig. 1 shows that each needle probe setup will be affected by magnetic flux variations in the air between the needle probes. Such effect must be minimized to avoid unwanted drift in the reconstructed hysteresis cycle. One way to achieve this is to print the needle probes directly on the sample surface [20]. Such probes are then fixed on the sample, which can be a limit since only one position is allowed. Needle probe setups can be realized with spring contact probes to ensure the contact between probes and sample, allowing for an easy positioning of the setup and for the scanning of the entire sample surface, but at the price of a greater air surface.

A. Preamble: Magnetic Fields Definition

The general definition for the magnetic induction vector $\vec{B}$ in the material is considered

$$\vec{B}(t) = \begin{bmatrix} B_x(t) \\ B_y(t) \\ B_z(t) \end{bmatrix}. \tag{2}$$

To enhance the readability of the equations, the time-derivative of the magnetic flux is noted $(d\Phi/dt)$:

$$\frac{d\Phi}{dt}(S) = \int\int_{S} \frac{\partial \vec{B}}{\partial t} \cdot \vec{n} dS. \tag{3}$$

Given a surface S of boundary ∂S, the induced voltage V_{ind} on ∂S can be calculated through Maxwell–Faraday's law as follows:

$$V_{\text{ind}} = \oint_{\partial S} \vec{E} \cdot \vec{dl} = -\frac{d\Phi}{dt}(S). \tag{4}$$

The surface S can be separated into air (S_{air}) and ferromagnetic sample (S_{sample}). Such decomposition is illustrated for

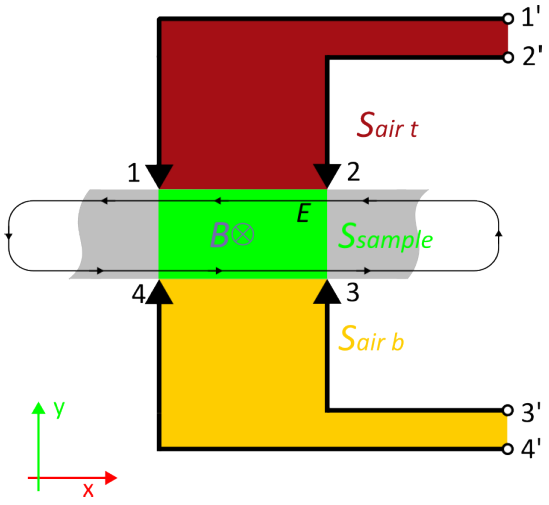

Fig. 2. Air and sample surfaces in the OS.

each setup in Figs. 2–6 and the resulting equation is given below

$$\frac{d\Phi}{dt}(S) = \frac{d\Phi}{dt}(S_{\text{air}}) + \frac{d\Phi}{dt}(S_{\text{sample}}). \tag{5}$$

A reasonable assumption is that the measurement device has an infinite impedance, hence, no current flows on the cables connecting the needle probes to the measurement device.

B. Original Setup

Considering a magnetic field $\vec{B}$ normal to the cross section S_{sample}, Fig. 2 shows the OS and the associated Maxwell–Faraday's surfaces S_{sample}, $S_{\text{air }t}$ and $S_{\text{air }b}$.

To obtain the magnetic flux variation inside the sample, two extra assumptions are made.

1) The effective vertical electric field V_{vert} is negligible

$$V_{\text{vert}=} V_{14} + V_{32} \approx 0. \tag{6}$$

2) The effective air flux term is negligible

$$\frac{d\Phi}{dt}(S_{\text{air }t}) + \frac{d\Phi}{dt}(S_{\text{air }b}) \approx 0. \tag{7}$$

These conditions are necessary to obtain an equation linking the magnetic flux change rate to the measured voltages, but they are rarely satisfied [14], [18]. If they are supposed true, then it is shown in the Supplementary Materials (Section S.I.A) that the magnetic flux variation is given by the sum of the two measured voltages $V_{1'2'}$ and $V_{3'4'}$

$$V_{1'2'} + V_{3'4'} \approx \frac{d\Phi}{dt}(S_{\text{sample}}). \tag{8}$$

C. Single-Side OS

In the case of the SSOS, only one of either $V_{1'2'}$ or $V_{3'4'}$ is available, while the same Maxwell–Faraday surfaces are defined. The setup is shown in Fig. 3.

To be able to solve such system, it must be assumed that the electric field at the surface of the sample (and hence the magnetic flux inside the sample) is symmetric with respect to the center of the cross section

$$V_{12} = V_{34}, \quad V_{23} = V_{41}. \tag{9}$$

By assuming that both (6) and (9) are verified, the simplified (8) shows that the magnetic flux variation is given by

$$V_{1'2'} \approx \frac{1}{2}\frac{d\Phi}{dt}(S_{\text{sample}}). \tag{10}$$

The main disadvantages of the SSOS compared to the OS is the halved gain in (10) and the additional assumption regarding the symmetry of the problem. The two techniques are sensitive to a magnetic flux variation in the air.

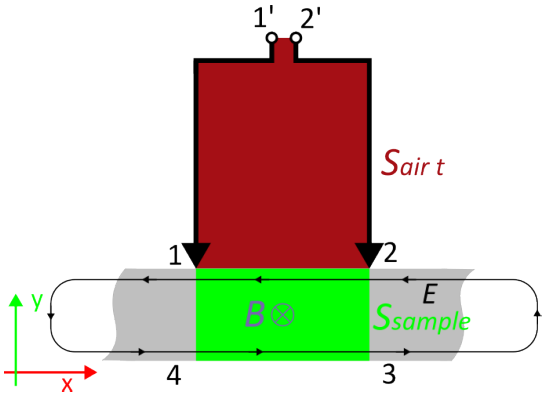

Fig. 3. Air and sample surfaces in the SSOS.

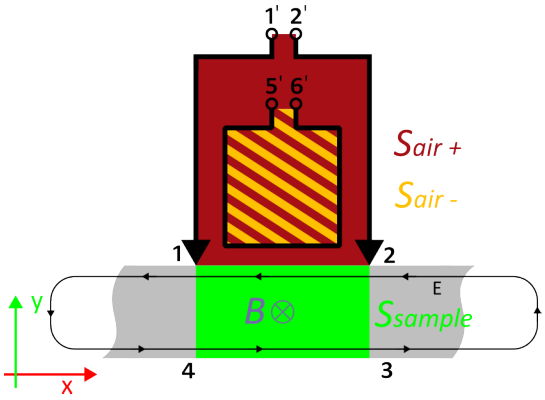

Fig. 4. Air and sample surfaces in the AFCS.

D. Air Flux Compensation Setup

The Maxwell–Faraday surfaces for the AFCS are shown in Fig. 4.

The only difference of this setup compared to the SSOS is that the "no air flux term" assumption is modified in "negligible air flux outside the air loop"

$$\frac{d\Phi}{dt}(S_{\text{air }+}) - \frac{d\Phi}{dt}(S_{\text{air }-}) \approx 0. \tag{11}$$

It is shown in the Supplementary Materials (Section S.I.B) that the measured voltages are linked to the magnetic flux

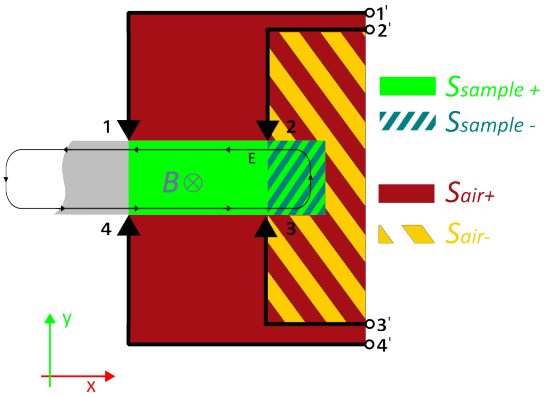

Fig. 5. Air and sample surfaces in the TNPS.

variation as follows:

$$V_{2'1'} - V_{6'5'} = -V_{\text{vert}} - \frac{d\Phi}{dt}(S_{\text{air }+}) + \frac{d\Phi}{dt}(S_{\text{air }-}) - \frac{1}{2}\frac{d\Phi}{dt}(S_{\text{sample}}). \tag{12}$$

Hence, the simplified AFCS equations can be obtained if (6) and (11) are verified

$$\begin{cases} V_{1'2'} - V_{5'6'} \approx \dfrac{1}{2}\dfrac{d\Phi}{dt}(S_{\text{sample}}) \\ V_{5'6'} = \dfrac{d\Phi}{dt}(S_{\text{air }-}). \end{cases} \tag{13}$$

The AFCS is equivalent to the SSOS, but with an effective air surface $S_{\text{air}} = S_{\text{air }+} - S_{\text{air }-}$. This setup allows to decrease the air flux term by decreasing the effective surface S_{air}. However, the vertical electric field can still be an issue, and the symmetry assumption requires a precise positioning of the needle probes.

E. Transverse Needle Probe Setup

Fig. 5 shows the Maxwell–Faraday surfaces for the TNPS. It is shown in the Supplementary Materials (Section S.I.C) that such setup is equivalent to the difference of two SSOS, defined by their measured voltages $V_{1'4'}$ and $V_{2'3'}$

$$V_{1'4'} - V_{2'3'} \approx \frac{d\Phi}{dt}(S_{\text{sample}}). \tag{14}$$

Such setup doubles the gain for the magnetic flux variation compared to the SSOS and is less impacted by the vertical field (since the two contributions are subtracted). It also allows to decrease the air surface (even if not as much as the AFCS). As a result, the TNPS can be employed for precise measurements. However, the needle probes need to be aligned on both sides of the sample, hence, the TNPS can be difficult to implement on plates and less practical than the AFCS for quick measurements.

F. Complete Needle Probe Setup

The ideal setup would allow to reduce both the air flux and the vertical electric field contributions to negligible levels. Hence, one could try to combine the AFCS and the TNPS to get the advantages of both. An improved system, the complete needle probe setup (CNPS), should then give accurate measurements. The setup is shown in Fig. 6.

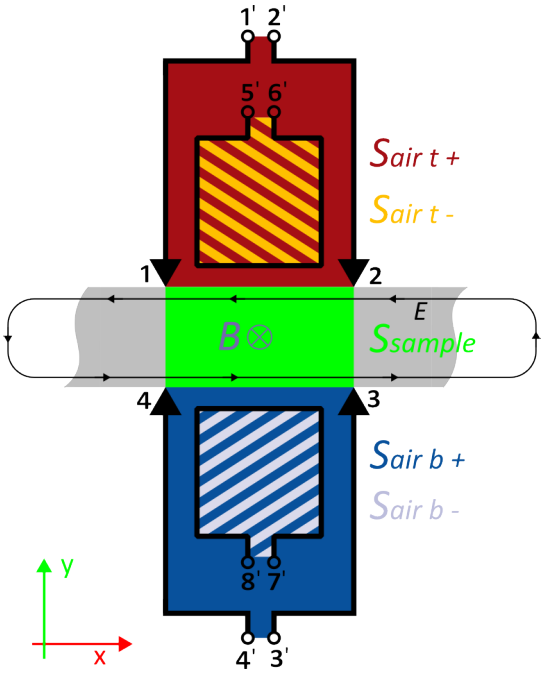

Fig. 6. Air and sample surfaces in the CNPS.

With the assumptions defined in the Supplementary Materials (Section S.I.D), four measurements allow to define the magnetic flux variation inside the sample

$$[V_{1'2'} - V_{5'6'}] + [V_{3'4'} - V_{7'8'}] \approx \frac{d\Phi}{dt}(S_{\text{sample}}). \tag{15}$$

The advantage of the CNPS is that it can be simplified to obtain five different measurements (OS and AFCS/SSOS for both sample surfaces) simply by choosing which subset of measured voltages to analyze, without moving the needle probes. This approach is illustrated in the experimental results shown in Section VII. The four measured voltages $V_{1'2'}$, $V_{3'4'}$, $V_{5'6'}$, and $V_{7'8'}$ can be measured at once, and they can therefore be investigated separately or together to identify dissymmetries in magnetic flux with respect to the depth and address any issue related to the air flux term. Significant differences between $V_{1'2'}$ and $V_{3'4'}$ reveal dissymmetries in the magnetic flux distribution. The air flux term can be identified by comparing the amplitudes of $V_{1'2'}$ and $V_{5'6'}$ (or of $V_{3'4'}$ and $V_{7'8'}$).

However, the CNPS requires to measure four voltages per axis (and therefore to carefully position four couples of needle probes). The amplifier for each input must be carefully calibrated to ensure a constant gain during the entire measurement and therefore the correct compensation of the air flux effect.

Alignment issues between the "top" and "bottom" needle probe holders can appear if the sample is a large slab or a tube, for which the alignment between the two probe holders cannot be verified by sight. In the case of curved surfaces, the equations linking the measured voltages to the magnetic flux variations will not be as straightforward as the ones shown in Sections II-B–II-F. The configuration with curved specimens

TABLE I
COMPARISONS BETWEEN THE FIVE NEEDLE PROBE SETUPS

Setup	Number of measures	Requires symmetry	Air flux effect
SSOS	**1**	Yes	Great
OS	2	**No**	Great
AFCS	2	Yes	**Small**
TNPS	2	**No**	Great
CNPS	4	**No**	**Small**

has not been investigated in this work, but a careful design of the complete system and the exploitation of spring test probes to ensure the contact between a curved surface and the needle probes should allow to overcome most experimental issues.

Table I compares the five different setups, showing the strengths and weaknesses of each one. The CNPS is the configuration requiring the highest number of measured voltages, but it is the only one weakly sensitive to both sample flux dissymmetry and air flux.

III. FE MODEL FOR THE NEEDLE PROBE MEASUREMENTS

A. Definition of the Modeled Problem

The experimental system was modeled using the FE method in COMSOL Multiphysics.[1] The setup is presented in Fig. 7. The measurement region size ($20 \times 20 \times 6$ mm^3) and location (at the center of the sample) fulfill the criteria (derived from [8]) for reliable magnetic measurements.

1) *Uniformity Criterion:* The direction and magnitude of $\vec{H}$ and $\vec{B}$ fields do not depend on the position of the sensor in the measurement regions.
2) *Correspondence Criterion:* The measured $\vec{H}$ field (outside the sample) corresponds to the $\vec{H}$ field inside the sample that generates the measured $\vec{B}$ field.
3) *Direction Criterion:* $\vec{H}$ and $\vec{B}$ fields directions are known.

The sample was meshed using a swept quadrangle mesh in the Z-axis and a boundary layer mesh in the Y-axis (with four elements in the skin depth). The rest of the geometry uses tetrahedral elements. The coils are modeled using a homogenized multiturn conductor model.

The material properties are given in Table II. Note that other configurations with different geometries (coils on the yoke legs, thinner sample, and shorter yokes) and material properties were studied. However, the conclusions drawn from such studies are identical to the ones presented here. The sample material is an Iron–Cobalt alloy, whose magnetization function $M(H)$ and parameters are taken from [24].

Simulated needle probe measurements are obtained by integrating the simulated electric field following the paths in Fig. 8 counterclockwise.

The simulated system is symmetrical and the needle probes are far enough from the sample edges to assume that the electric field on the cross section is horizontal. This implies that the vertical voltages V_l and V_r are negligible and opposite ($V_l + V_r \approx 0$), hence, the voltage measured on a virtual

[1]Trademarked.

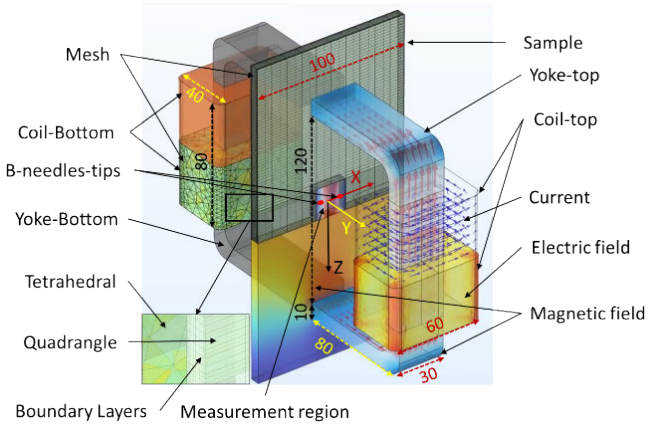

Fig. 7. Simulated structure on COMSOL. Dimensions are in mm.

TABLE II
ELECTROMAGNETIC PROPERTIES USED IN THE FE MODEL

Properties	Yoke	Coil	Sample
Electric conductivity (MS/m)	1	6	3
Relative permittivity	1	1	1
Relative magnetic permeability	10^4	1	Non-linear [24]

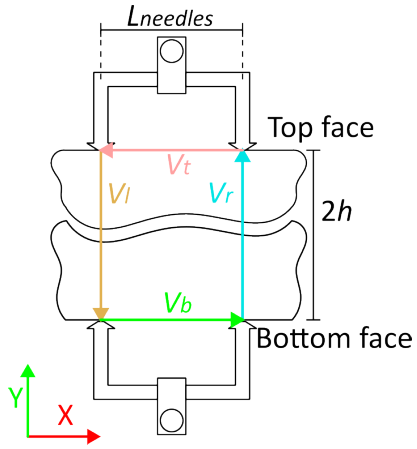

Fig. 8. Integration paths employed for the needle probes and wrapping coil voltages.

wrapping coil following the path on Fig. 8 is obtained by summing V_t and V_b:

$$V_{\text{coil}} \approx V_t + V_b. \tag{16}$$

If the setup is not symmetrical (as detailed in the next paragraphs), then V_t will not be identical to V_b, hence, an asymmetry factor ϵ_{ASYM} can be defined

$$\epsilon_{\text{ASYM}}(\%) \approx 100 \sqrt{\frac{\int_0^T [V_t(t) - V_b(t)]^2 dt}{\int_0^T V_{\text{coil}}^2(t) dt}}. \tag{17}$$

Simulations are carried out for a duration $T = (1/4 f_{\text{exc}})$, f_{exc} being the excitation frequency. This implies that only the first magnetization curve of the material is simulated to keep reasonable simulation times.

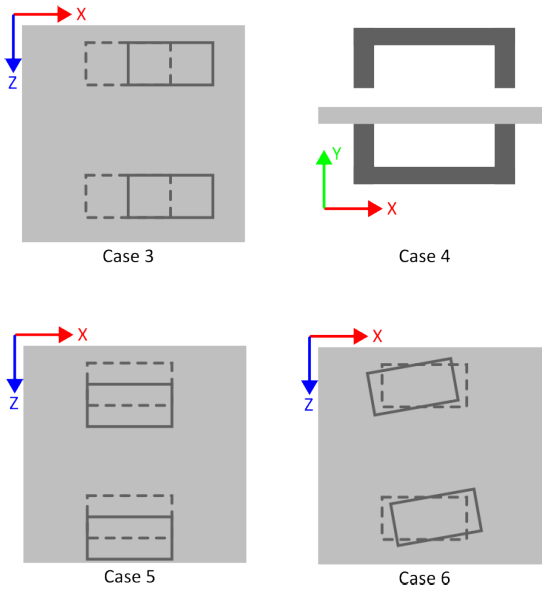

Fig. 9. Yoke displacement described in cases 3–6.

TABLE III
ASYMMETRY FACTOR IN DIFFERENT SIMULATION CASES

Case	0	1	2	3	4	5	6
$\epsilon_{ASYM}(\%)$	0.16	**8.41**	0.61	0.27	**2.92**	0.25	0.23

B. Geometrical Asymmetry

One way to introduce asymmetry in the through-thickness magnetic flux is to break the symmetry of the excitation system (coils and yoke). Several examples have been tested with $f_{exc} = 1$ Hz.

1) *Case 0:* Two excitation yokes (perfectly symmetrical), chosen as reference.
2) *Case 1:* One excitation yoke.
3) *Case 2:* Two excitation yokes, with one yoke generating 10% more magnetic flux compared to the other.
4) *Case 3:* Two excitation yokes, one yoke being moved 5 mm in the X-direction.
5) *Case 4:* Two excitation yokes, one yoke being moved 5 mm in the Y-direction (normal to the sample surface).
6) *Case 5:* Two excitation yokes, one yoke being moved 5 mm in the Z-direction.
7) *Case 6:* Two excitation yokes, one yoke being rotated of 10° compared to the other one.

Cases 3–6, showing the modification of the position of the yokes for each case, are illustrated on Fig. 9 and the resulting asymmetry factors are shown in Table III.

It can first be noticed that the asymmetry coefficient is not zero in the symmetric case. This is due to residual dissymmetries in the meshes. The value of 0.16% for ϵ_{ASYM} can be taken as the reference for negligible asymmetry. Among the studied cases, a strong asymmetry is generated by an asymmetric magnetic excitation, with either one yoke or two yokes with a detectable liftoff for one of them. A current asymmetry (as in Case 2) should not have a great effect on the asymmetry if the two excitation currents are similar enough, and a misalignment for the two yokes in the sample surface directions should not be noticeable.

Hence, using two identical yokes with similar excitation coils (in terms of coil turns and surface) connected in series and ensuring that liftoff is minimal should reduce the flux asymmetry to acceptable levels.

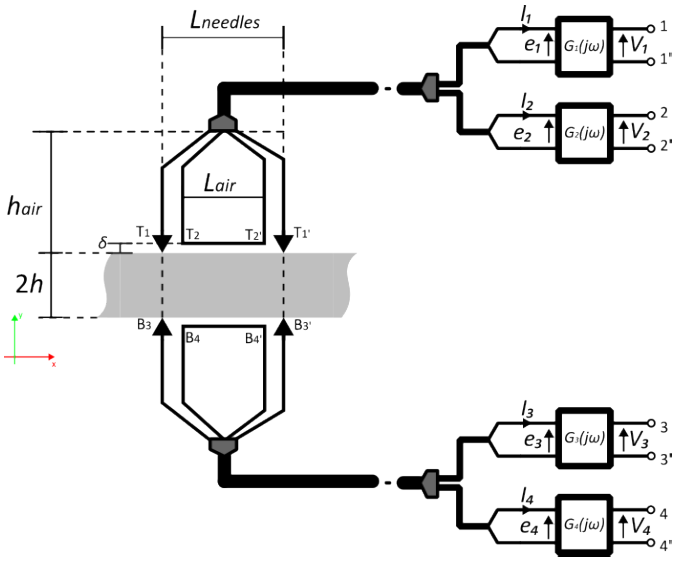

Fig. 10. Proposed setup with the geometric dimensions and the analog treatment circuits.

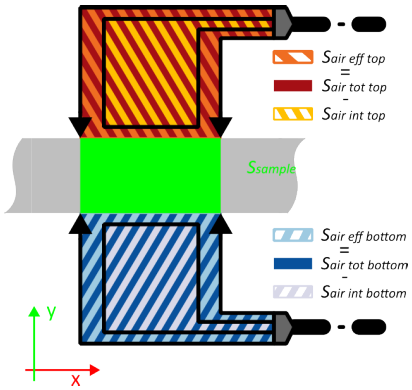

Fig. 11. Maxwell–Faraday surfaces in the proposed setup. All surfaces beyond the coaxial cable are ignored.

IV. Data Treatment: From the Measured Voltages to the Magnetic Induction for the Proposed Setup

This section describes the different steps required to obtain the magnetic flux variation from the measured voltages for the CNPS (similar equations can be found for the simpler setups). The complete setup is shown in Fig. 10, and the Maxwell–Faraday surfaces are shown in Fig. 11.

The connection wires for the measured signals are grouped in a thick coaxial cable. The voltage e_i is the voltage measured in the loop containing the points T_i and $T_{i'}$ for the "top" face, and B_i and $B_{i'}$ for the "bottom" face. Each voltage is also amplified by an analog circuit of transfer function $G_i(j\omega)$ (with ω the angular frequency).

The general equation for this setup is developed in the Supplementary Materials (Section S.II) and is simplified thanks to the following assumptions.

1) *Assumption 1:* The amplification circuits on all inputs are perfect, each one with a gain G_i for all frequencies

$$V_i = G_i e_i. \tag{18}$$

2) *Assumption 2:* Input impedances are infinite (or, in other words, no current flows in the connections between the needle probes and the amplification circuit)

$$I_i = 0. \tag{19}$$

3) *Assumption 3:* The liftoff δ between the "air" needle probes and the sample surface is negligible

$$\delta \to 0. \tag{20}$$

4) *Assumption 4:* The magnetic flux far from the sample is negligible compared to the magnetic flux near the surface

$$\left|\frac{\partial B_n}{\partial t}\right|(|y| \to h + h_{\text{air}}) \ll \left|\frac{\partial B_n}{\partial t}\right|(|y| \to h). \tag{21}$$

5) *Assumption 5:* The magnetic flux is uniform on the X-axis

$$\frac{d\Phi}{dt}(S_{\text{sample}}) = L_{\text{needles}} \int_{-h}^{h} \frac{\partial B_n}{\partial t}(y)dy \tag{22}$$

$$\frac{d\Phi}{dt}(S_{\text{air int top}}) = L_{\text{air}} \int_{h+\delta}^{h_{\text{air}}} \frac{\partial B_n}{\partial t}(y)dy \tag{23}$$

$$\frac{d\Phi}{dt}(S_{\text{air int bottom}}) = L_{\text{air}} \int_{-h_{\text{air}}}^{-h-\delta} \frac{\partial B_n}{\partial t}(y)dy. \tag{24}$$

By combining these assumptions, the magnetic flux variation in the sample is given by

$$\frac{d\Phi}{dt}(S_{\text{sample}}) \approx -\left(\frac{V_1}{G_1} - \frac{L_{\text{needles}}}{L_{\text{air}}}\frac{V_2}{G_2}\right) + \left(\frac{V_3}{G_3} - \frac{L_{\text{needles}}}{L_{\text{air}}}\frac{V_4}{G_4}\right). \tag{25}$$

The *B(H)* curve is then obtained by integrating the previous equation, with the assumption that the magnetic induction is uniform inside the sample

$$B(t) \approx \frac{1}{S_{\text{sample}}} \int_0^t \frac{d\Phi}{ds}(S_{\text{sample}})ds. \tag{26}$$

This equation is the general case for all magnetic needle probe setups except the TNPS, and can be simplified for each elementary setup seen previously.

V. Error Sources in the Magnetic Induction Measurement (Uniaxial Excitation Case)

The relationship between magnetic induction change and measured voltages seen above can also be employed to detect several error sources for the hysteresis loop reconstruction. Such measurements are obtained by placing two pairs of needle probes perpendicular to each other (unless specified otherwise). The magnetic flux is supposed uniform on the entirety of the cross section and along the Z-direction.

Different error sources have been analyzed in the Supplementary Materials (Section S.III).

1) The needle probe position errors include the position errors between the "top" and "bottom" sample needle probes due to a misalignment of the needles support. Such position errors can be a translation error (Δx and Δz) and a rotation error ($\Delta\beta$). Only the latter has an effect on the experimental measurement if the magnetic flux is uniform. The resulting error can be ignored if $|\Delta\beta| < 14°$, which should be the case in the great majority of cases.
2) The air needle probes liftoff concerns the presence of a liftoff δ between the sample surface and the air needle probes. The analytical expression of this error cannot be easily calculated, since it heavily depends on $B_n(y)$. However, since $B_n(y)$ should quickly converge toward 0 far enough from the sample surface, even small values of δ will significantly decrease the measured air flux voltage. Hence, the resulting *B(H)* loops will be affected by an increased drift at saturation if the air needle probes liftoff is not minimized.
3) The air-sample angle mismatch concerns the position errors between the "sample" and the "air" needle probes on the same sample surface. As with the needle probes position errors, only the angular error γ affects the experimental measurements and, like the air needle probes liftoff, it will result in an increased drift at saturation for the *B(H)* loops. This error evolves in $1 - \cos(\gamma)$, hence, it should be considered only in presence of major alignment issues on the experimental setup.
4) The gain mismatch ΔG and the nonorthogonality angle $\Delta\alpha$ include the gain differences for the amplification circuits and the alignments issues between the X and the Z needle probes. Such effects can be corrected in posttreatment with two different measurements carried out at different positions.

As long as the experimental setup is manufactured with precision (such as by 3-D printing the needle probes support), all these errors should be either negligible or easily corrected in posttreatment.

VI. Experimental Setup

The easiest way to compare the needle probes and the wrapping coil measurements is through a classical single-sheet tester (SST) measurement. In this case, the magnetic field is generated through one pair of yokes and hence both $\vec{H}$ and $\vec{B}$ are supposed 1-D

$$\vec{H} = H(t)\vec{e_Z}. \tag{27}$$

The experimental setup is shown in Fig. 12. Two types of samples have been tested: DC04 steel [25] and Galfenol [26].

As in the FE model, two identical iron–silicon yokes have been employed to obtain a symmetrical magnetic excitation (the two excitation coils have 106 ± 3 turns). Both excitation coils are connected to a Kepco BOP72-14MG bipolar power source (with a maximal current of 14 A and a maximal voltage

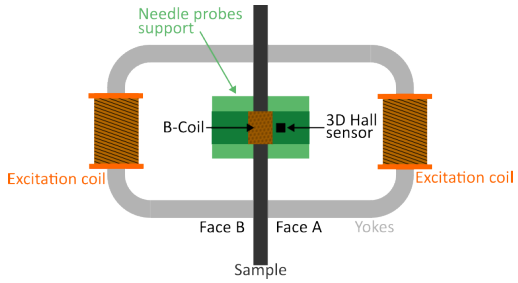

Fig. 12. Experimental setup employed for needle probes and wrapping coil measurements.

TABLE IV
EXPERIMENTAL SETUP PARAMETERS

Parameter	Description	Value
$2h$ (mm)	Fig. 14	2 ± 0.2
$2L$ (mm)	Fig. 14	20 ± 0.5
δ (mm)	Fig. 10	2 ± 0.5
h_{air} (mm)	Fig. 10	35 ± 1
$\Delta G(\%)$	Fig. 10	< 1
$\Delta\alpha$ (°)	Fig. 10	< 2
L_{inner} (mm)	Fig. 14	20 ± 0.5
L_{outer} (mm)	Fig. 14	25 ± 0.5
β (°)	Fig. 14	45 ± 1

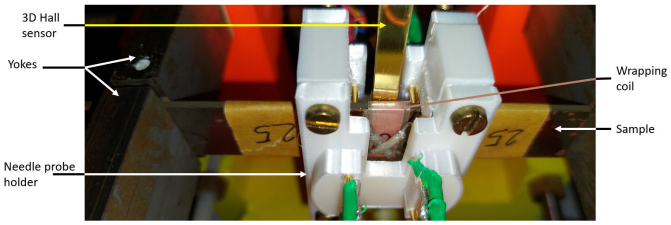

Fig. 13. Needle probe holder mounted on the sample between the yokes.

of 72 V). The magnetic field is measured using a Projekt Elektronik AS-V3DM Hall sensor, allowing a 3-D measurement with an estimated error of 4 A/m and an estimated liftoff of 1 mm. The sampling frequency is 5 kHz. More details about the excitation generation and control can be found in [27]. The geometric dimensions and the error parameters are given in Table IV.

The magnetic induction is measured with the proposed needle probe setup and compared to the signal of a wrapping coil of 25 (for the DC04 sample) or 30 (for the Galfenol sample) turns, wound as tightly as possible to the sample to minimize the induced voltage generated by the magnetic flux outside the sample. A specific sensor has been designed and 3-D-printed in order to read the magnetic induction through the needle probes at the same place as the wrapping coil. A photo and a drawing of the holder are shown in Figs. 13 and 14. The "inner" needle probes are short-circuited above the wrapping coil to measure the air flux, while the "outer" needle probes touch the sample. The needle probes have been rotated by an angle β in order to fit the wrapping coil between the needle probes to ensure that both systems measure the magnetic induction variation in the same area.

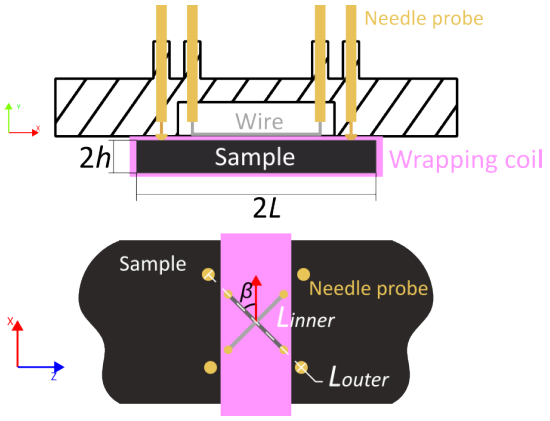

Fig. 14. Schematics of the needle probe holder and the probe connections.

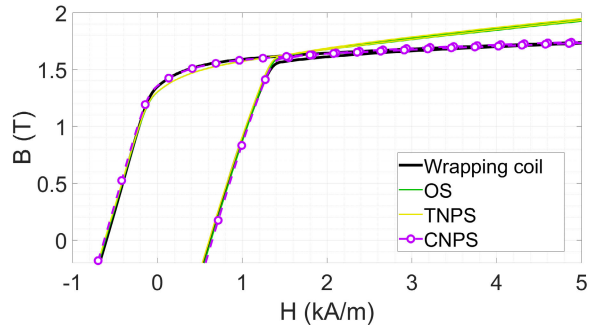

(a)

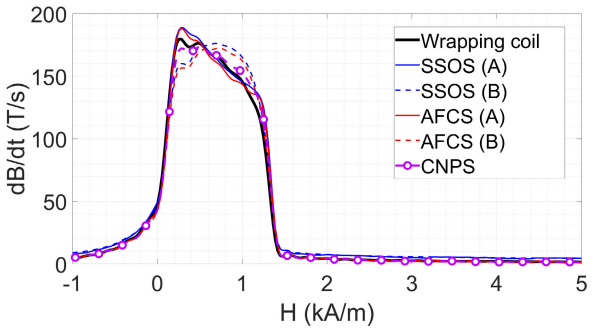

(b)

Fig. 15. Experimental hysteresis loops and *dB/dt(H)* measured through different needle probe setups, and comparison to the wrapping coil hysteresis loop for the DC04 sample. (a) *B(H)*. (b) *dB/dt(H)*.

VII. EXPERIMENTAL MEASUREMENTS

The measured hysteresis loops for both DC04 and Galfenol samples have been carried out with $f_{\text{exc}} = 1$ Hz. Figs. 15 and 16 show the experimental hysteresis loops through the symmetric setups (CNPS, OS, and TNPS) and the measured *dB/dt* for the asymmetric setups (SSOS and AFCS). For both figures, all signals are compared to the measurements from the wrapping coil, taken as a reference method. The signals being symmetrical with respect to the Y-axis, only the upper section of the functions is shown to increase the readability of the figures.

The air flux term is clearly noticeable on all experimental measurements for the chosen needle probes support, since all setups without air flux compensation (OS and TNPS) show a clear drift after the magnetic saturation. The results

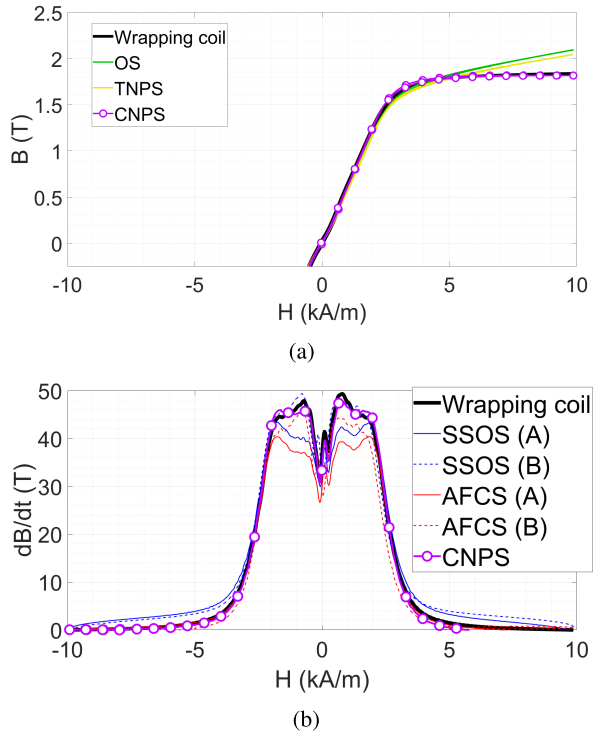

Fig. 16. Experimental hysteresis loops and *dB/dt(H)* measured through different needle probe setups, and comparison to the wrapping coil hysteresis loop for the Galfenol sample. (a) *B(H)*. (b) *dB/dt(H)*.

obtained from the asymmetric setups (SSOS and AFCS) are also different depending on the chosen face (A or B), such effect being more noticeable on the *dB/dt* measurements. Such asymmetry is linked to the material, since the magnetic excitation system is symmetric. It is not attempted here to explain the presence of this asymmetry, an asymmetrical residual stress distribution being one possible reason, as seen in Section S.IV. However, the proposed setup gives access to this asymmetry, allowing for a more complete measurement than the wrapping coil setup. The asymmetry coefficient ϵ_{ASYM} for each measurement, calculated according to (17) is given in Table V.

For more quantitative comparisons between the curves, two indicators are employed: the relative Euclidean difference (RED) and the maximum difference (MD). These factors will be 0 if two curves are identical, and the greater their value, the greater the differences. Given two arrays (the reference x and the measured curve y) of size N, their RED and MD are defined as

$$\text{RED}(\%) = 100\sqrt{\frac{\sum_{i=1}^{N}(x[i]-y[i])^2}{\sum_{i=1}^{N}x[i]^2}} \tag{28}$$

$$\text{MD}(\%) = 100\frac{\max|x-y|}{\max|x|}. \tag{29}$$

Tables VI–IX show the RED and MD between the wrapping coil data (*B(H)* and *dB/dt(H)* and the measured data with each needle probe setup. Both indicators have been calculated for each one of 20 cycles, allowing to determine the variation on RED and MD, their average and their standard deviation (SD).

TABLE V
EXPERIMENTAL ASYMMETRY COEFFICIENTS FOR THE MEASUREMENTS

Sample	Setup	ϵ_{ASYM} (%)
DC04	**AFCS**	5.60
DC04	**SSOS**	5.35
Galfenol	**AFCS**	6.07
Galfenol	**SSOS**	5.52

TABLE VI
RED (%) FOR EACH SETUP FOR THE TWO SAMPLES (*B*)

	DC04			Galfenol		
Setup	Min/Max	Average	SD	Min/Max	Average	SD
CNPS	0.78 / 1.00	0.86	0.07	0.91 / 1.11	0.99	0.06
TNPS	23.39 / 23.80	23.61	0.09	21.74 / 22.06	21.91	0.09
OS	22.58 / 22.91	22.74	0.07	24.43 / 24.82	24.64	0.11
SSOS A	22.52 / 22.88	22.69	0.08	23.68 / 23.99	23.84	0.09
SSOS B	22.65 / 22.90	22.78	0.07	25.21 / 25.73	25.51	0.13
AFCS A	2.38 / 2.59	2.46	0.06	2.35 / 2.56	2.44	0.07
AFCS B	2.84 / 3.15	2.96	0.10	4.49 / 5.08	4.72	0.16

TABLE VII
RED (%) FOR EACH SETUP FOR THE TWO SAMPLES (*dB/dt*)

	DC04			Galfenol		
Setup	Min/Max	Average	SD	Min/Max	Average	SD
CNPS	5.80 / 5.94	5.88	0.05	4.11 / 4.38	4.24	0.07
TNPS	9.88 / 11.70	10.63	0.67	13.61 / 14.04	13.82	0.11
OS	9.81 / 9.87	9.84	0.02	15.21 / 15.39	15.28	0.04
SSOS A	10.23 / 10.31	10.24	0.02	16.27 / 16.60	16.38	0.07
SSOS B	12.24 / 12.38	12.30	0.03	16.47 / 16.90	16.64	0.12
AFCS A	6.45 / 6.71	6.61	0.09	8.07 / 8.15	8.10	0.02
AFCS B	9.40 / 9.52	9.46	0.04	6.99 / 7.36	7.14	0.09

TABLE VIII
MD (%) FOR EACH SETUP FOR THE TWO SAMPLES (*B*)

	DC04			Galfenol		
Setup	Min/Max	Average	SD	Min/Max	Average	SD
CNPS	3.29 / 3.77	3.53	0.14	2.42 / 3.13	2.75	0.22
TNPS	31.03 / 31.31	31.17	0.07	28.14 / 28.48	28.28	0.10
OS	29.86 / 30.16	30.00	0.08	31.33 / 31.68	31.48	0.11
SSOS A	29.84 / 30.14	29.98	0.08	30.91 / 31.26	31.06	0.11
SSOS B	29.87 / 30.17	30.01	0.07	31.75 / 32.10	31.90	0.11
AFCS A	2.92 / 3.17	3.03	0.06	3.45 / 3.69	3.57	0.07
AFCS B	6.07 / 7.28	6.71	0.32	6.34 / 7.94	7.07	0.47

TABLE IX
MD (%) FOR EACH SETUP FOR THE TWO SAMPLES (*dB/dt*)

	DC04			Galfenol		
Setup	Min/Max	Average	SD	Min/Max	Average	SD
CNPS	8.29 / 8.62	8.39	0.09	5.17 / 6.04	5.61	0.24
TNPS	10.13 / 15.35	12.88	2.36	11.88 / 15.43	13.19	1.03
OS	10.21 / 10.40	10.31	0.05	12.22 / 12.64	12.41	0.15
SSOS A	14.92 / 15.45	15.28	0.13	14.75 / 26.26	16.02	2.58
SSOS B	12.20 / 13.73	12.41	0.32	15.49 / 17.63	15.87	0.50
AFCS A	12.43 / 13.10	12.63	0.18	11.32 / 12.90	12.16	0.48
AFCS B	14.36 / 14.61	14.49	0.07	6.35 / 7.32	6.89	0.23

For both materials, the hysteresis loop given by the proposed setup closely matches the wrapping coil measurement, while the drift generated by the air flux heavily impacts the setup without air flux compensation (TNPS, OS, and SSOS). The air flux brings a supplementary voltage directly proportional to (dH/dt), and, once integrated, it creates a linear drift on the *B(H)* figures for these setups. The AFCS gives similar results to the proposed setup, but with a noticeable variability of the

measure depending on the chosen face for the measurement (A or B).

VIII. Conclusion

The needle probe technique is a good candidate for magnetic induction measurements thanks to its simple positioning, requiring only to move the needle probe holder to modify the position and the direction of the measurement. Therefore, the requirements on the shape of the sample to test are more flexible compared to wrapping coil measurements. For the latter, the sample needs to be long and thin, while the needle probe technique only requires the sample to have a conductive surface. Magnetic induction measurements can be carried on slabs, and two orthogonal pairs of needle probes can be employed to ensure 2-D measurements of the magnetic flux variations in the sample. Moreover, the needle probes can be deployed on a slab without the need to drill holes (which significantly affect the microstructural state of the material).

This article presents several needle probe setups, with some already described in the literature and whose strong and weak points are not only known, but also describes a novel setup. Even if a greater number of inputs is required to acquire all the useful signals, this setup combines the advantages of the previous setups, namely the reduction of the air flux term and the fact that flux symmetry is not required for further data treatment. Moreover, measurements sensitive to flux asymmetries can be implemented, thus allowing a more thorough study of the magnetic flux distribution compared to wrapping coils setups.

Furthermore, several uncertainty sources have been studied through both numerical and analytical approaches. Dual yokes are required (with their liftoff minimized) to minimize flux asymmetries generated by the setup, and simple algorithms are available to fix the other error sources once they have been measured by a calibration measurement. After correction of the uncertainty sources, the proposed setup gives the same measurements in a 1-D-configuration as the wrapping coil with a RED smaller than 1.2%. Hence, the proposed setup can replace the wrapping coil system for experimental setups where the latter is too complex to deploy or where its deployment alters the flux distribution. Examples of such configurations are the measurement of magnetic induction on slabs and hollow pieces.

This study allows defining guidelines for the implementation of the needle probe technique for magnetic field measurements. It is notably shown that the following aspects should be considered carefully.

1) The air flux term adds an important drift to the experimental measurements, hence, its correction is necessary, either by minimizing the effective air surface or by directly measuring the induced voltage in that surface.
2) The gain and dephasing brought by analog amplifiers and filters must be precisely measured to minimize distortions.
3) High-frequency measurements affect the magnetic flux uniformity through the skin effect and bring both heat and mechanical vibrations, hence, caution must be taken when comparing the needle probe technique to the reference wrapping coil method.
4) The contact between the needle probes and the sample surface must be ensured at all times.

Provided that a careful implementation is performed, the needle probe technique is a very powerful tool for accurate magnetic induction measurements, with limited restrictions on the geometry of the inspected specimens.

References

[1] N. Soltau, D. Eggers, K. Hameyer, and R. W. De Doncker, "Iron losses in a medium-frequency transformer operated in a high-power DC–DC converter," *IEEE Trans. Magn.*, vol. 50, no. 2, pp. 953–956, Feb. 2014.

[2] Y. Li, X. Yan, C. Wang, Q. Yang, and C. Zhang, "Eddy current loss effect in foil winding of transformer based on magneto-fluid-thermal simulation," *IEEE Trans. Magn.*, vol. 55, no. 7, pp. 1–5, Jul. 2019.

[3] S. Tumanski, "Induction coil sensors—A review," *Meas. Sci. Technol.*, vol. 18, no. 3, pp. R31–R46, 2007.

[4] S. Zurek and T. Meydan, "Rotational power losses and vector loci under controlled high flux density and magnetic field in electrical steel sheets," *IEEE Trans. Magn.*, vol. 42, no. 10, pp. 2815–2817, Oct. 2006.

[5] S. Zurek, "Systematic measurement errors of local B-coils due to holes," *Przegląd Elektrotechniczny*, vol. 1, no. 3, pp. 8–14, Mar. 2018. [Online]. Available: http://sigma-not.pl/publikacja-112446-2018-3.html

[6] U. Aydin et al., "Rotational single sheet tester for multiaxial magneto-mechanical effects in steel sheets," *IEEE Trans. Magn.*, vol. 55, no. 3, pp. 1–10, Mar. 2019. [Online]. Available: https://ieeexplore.ieee.org/document/8611295/

[7] C. Delaunay, C. Joubert, and F. Sixdenier, "Behaviour of electrical steels under rotational magnetization and high temperatures," *J. Magn. Magn. Mater.*, vol. 590, Jan. 2024, Art. no. 171680.

[8] A. Abderahmane and L. Daniel, "Measurement criteria for the magnetic characterization of magnetic materials," *IEEE Trans. Instrum. Meas.*, vol. 72, pp. 1–18, 2023.

[9] E. Czeija and R. Zawischa, "Vorrichtung zum messen des wechselinduktionsflusses oder der flußänderung in ferromagnetischen materialien aus der induktionsspannung," Patent AT 180 990 B, Feb. 10, 1955.

[10] E. Werner, "Einrichtung zur messung magnetischer eigenschaften von blechen bei wechselstrommagnetisierung," Patent AT 191 015 B, Jul. 25, 1957.

[11] L. H. Stauffer, "Methods of and device for determining the magnetic properties of specimens of magnetic material," Patent 2 828 467, Mar. 25, 1958.

[12] R. E. Tompkins, L. H. Stauffer, and A. Kaplan, "New magnetic core loss comparator," *J. Appl. Phys.*, vol. 29, no. 3, pp. 502–503, Mar. 1958.

[13] T. Yamaguchi, K. Senda, M. Ishida, K. Sato, A. Honda, and T. Yamamoto, "Theoretical analysis of localized magnetic flux measurement by needle probe," *Le J. Phys. IV*, vol. 8, pp. Pr2-717–Pr2-720, Jun. 1998.

[14] G. Loisos and A. J. Moses, "Critical evaluation and limitations of localized flux density measurements in electrical steels," *IEEE Trans. Magn.*, vol. 37, no. 4, pp. 2755–2757, Jul. 2001.

[15] M. De Wulf, L. Dupré, D. Makaveev, and J. Melkebeek, "Needle-probe techniques for local magnetic flux measurements," *J. Appl. Phys.*, vol. 93, no. 10, pp. 8271–8273, May 2003.

[16] H. Pfutzner and G. Krismanic, "The needle method for induction tests: Sources of error," *IEEE Trans. Magn.*, vol. 40, no. 3, pp. 1610–1616, May 2004.

[17] G. Crevecoeur, L. Dupre, L. Vandenbossche, and R. Van de Walle, "Local identification of magnetic hysteresis properties near cutting edges of electrical steel sheets," *IEEE Trans. Magn.*, vol. 44, no. 6, pp. 1010–1013, Jun. 2008.

[18] A. A.-E. Abdallh, P. Sergeant, G. Crevecoeur, L. Vandenbossche, L. Dupré, and M. Sablik, "Magnetic material identification in geometries with non-uniform electromagnetic fields using global and local magnetic measurements," *IEEE Trans. Magn.*, vol. 45, no. 10, pp. 4157–4160, Oct. 2009.

[19] Y. A. T. Deffo, P. Tsafack, B. Ducharne, B. Gupta, A. Chazotte-Leconte, and L. Morel, "Local measurement of peening-induced residual stresses on iron nickel material using needle probes technique," *IEEE Trans. Magn.*, vol. 55, no. 7, pp. 1–8, Jul. 2019.

[20] B. Ducharne, Y. A. T. Deffo, P. Tsafack, and S. H. N. Kouakeuo, "Directional magnetic Barkhausen noise measurement using the magnetic needle probe method," *J. Magn. Magn. Mater.*, vol. 519, Feb. 2021, Art. no. 167453.
[21] W. Brix, K. Hempel, and F. Schulte, "Improved method for the investigation of the rotational magnetization process in electrical steel sheets," *IEEE Trans. Magn.*, vol. MAG-20, no. 5, pp. 1708–1710, Sep. 1984.
[22] S. Imamori, S. Aihara, H. Shimoji, A. Kutsukake, and K. Hameyer, "Evaluation of local magnetic degradation by interlocking electrical steel sheets for an effective modelling of electrical machines," *J. Magn. Magn. Mater.*, vol. 500, Apr. 2020, Art. no. 166372.
[23] M. Enokizono, I. Tanabe, and T. Kubota, "Localized distribution of two-dimensional magnetic properties and magnetic domain observation," *J. Magn. Magn. Mater.*, vol. 196, pp. 338–340, May 1999.
[24] L. Daniel, "An analytical model for the effect of multiaxial stress on the magnetic susceptibility of ferromagnetic materials," *IEEE Trans. Magn.*, vol. 49, no. 5, pp. 2037–2040, May 2013.
[25] M. Domenjoud and L. Daniel, "Effects of plastic strain and reloading stress on the magneto-mechanical behavior of electrical steels: Experiments and modeling," *Mech. Mater.*, vol. 176, Jan. 2023, Art. no. 104510.
[26] M. Domenjoud, A. Pecheux, and L. Daniel, "Characterization and multiscale modeling of the magneto-elastic behavior of galfenol," *IEEE Trans. Magn.*, vol. 59, no. 11, pp. 1–5, Nov. 2023.
[27] M. Domenjoud, E. Berthelot, N. Galopin, R. Corcolle, Y. Bernard, and L. Daniel, "Characterization of giant magnetostrictive materials under static stress: Influence of loading boundary conditions," *Smart Mater. Struct.*, vol. 28, no. 9, Sep. 2019, Art. no. 095012.
[28] M. Mahmoodi, M. Sedighi, and D. A. Tanner, "Investigation of through thickness residual stress distribution in equal channel angular rolled Al 5083 alloy by layer removal technique and X-ray diffraction," *Mater. Des.*, vol. 40, pp. 516–520, Sep. 2012.

Patrick Fagan received the Ph.D. degree in electric engineering (with a focus on magnetic NDT) from INSA Lyon, Villeurbanne, France, in 2022.

He is currently a Post-Doctoral Researcher with the Laboratoire de Génie Électrique et Électronique de Paris, Gif-sur-Yvette, France. His research interests include the experimental deployment of NDT techniques, analog signal treatment, and ferromagnetic materials characterization.

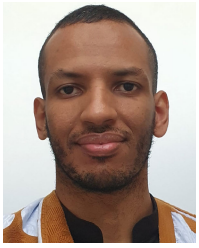

Abdellahi Abderahmane received the degree in mechanical engineering from the University of Tunis El Manar, Tunis, Tunisia, in 2016, and the master's degree in acoustical engineering and the Ph.D. degree in electrical engineering from Université Paris-Saclay, Gif-sur-Yvette, France, in 2017 and 2021, respectively.

He is currently a Post-Doctoral Researcher with the Group of Electrical and Electronic Engineering of Paris (GeePs), Université Paris-Saclay. His research interests include electromagnetic numerical simulation, nondestructive testing, tomographic imaging, and characterization of ferromagnetic materials.

Mathieu Domenjoud received the M.Sc. degree in electrical engineering from the University of Tours, Tours, France, in 2008, and the Ph.D. degree in electrical engineering with a focus on the characterization of electro-acoustic properties of piezoelectric structures under electrical and mechanical stress, from the GREMAN Laboratory, University of Tours, in 2012.

He became an Assistant Professor with the IUT of Cachan, Université Paris-Saclay, Gif-sur-Yvette, France, in 2014, where he joined the Group of Electrical Engineering of Paris (GeePs). His main research interests include the characterization of electro-magneto-mechanical couplings, the definition of constitutive laws by phenomenological approaches, and the prediction of such coupled phenomena by considering multiscale methods.

Laurent Daniel received the Ph.D. degree from the École Normale Supérieure de Cachan, Cachan, France, in 2003, and the Habilitation degree in physics from Université Paris-Sud, Orsay, France, in 2011.

Since 2015, he has been a Full Professor with CentraleSupélec, Université Paris-Saclay, Gif-sur-Yvette, France. His research interests, within the Laboratoire de Génie Électrique et Électronique de Paris, Paris, France, are dedicated to electromechanical and magnetomechanical couplings in materials for electrical engineering applications. He is notably involved in the definition of multiscale methods for the prediction of such coupled phenomena and in the development of dedicated experimental characterization setups.